Phase transitions in tridymite studied using 'Rigid Unit Mode' theory, Reverse Monte Carlo methods and molecular dynamics simulations

M. T. Dove[1,*], A. K. A. Pryde[1] and D. A. Keen[2]

[1] Department of Earth Sciences, University of Cambridge, Downing Street, Cambridge CB2 3EQ, UK
[2] ISIS Facility, Rutherford Appleton Laboratory, Chilton, Didcot, Oxfordshire OX11 0QX, UK

ABSTRACT

The phase transitions in tridymite and the nature of the high-temperature phase are investigated using a combination of Rigid Unit Mode theory, neutron total scattering measurements analysed using the Reverse Monte Carlo method, and molecular dynamics simulations. The unusually large number of phase transitions in tridymite can be explained within the Rigid Unit Mode theory. The Rigid Unit Mode theory also gives an interpretation of the disordered high-temperature phase as revealed by the neutron scattering data and the molecular dynamics simulations. There is a close correspondence between the structure of the disordered high-temperature phase of tridymite and that of β-cristobalite.

Keywords: tridymite, phase transitions, molecular dynamics, neutron total scattering, reverse Monte Carlo.

Introduction

ALTHOUGH many silicate and aluminosilicate crystals undergo displacive phase transitions on changing temperature, the tridymite polymorph of silica is notable for the remarkable number of displacive phase transitions that occur at ambient pressure (de Dombal and Carpenter, 1993; Cellai *et al.*, 1994; Pryde and Dove, 1998). The established equilibrium sequence of phase transitions is illustrated in Fig. 1, and the crystal structures of some of the equilibrium phases are shown in Fig. 2, but there are other phase transitions that can occur in samples of tridymite due to stacking faults, defects or small grain size.

The large number of displacive phase transitions found in tridymite is seen to be even more notable by comparison with the cristobalite phase of silica, which has a similar crystal structure but only one displacive phase transition at ambient pressure. The structures of both tridymite and cristobalite are based on identical layers of 6-membered rings of SiO_4 tetrahedra, with alternative tetrahedra pointing in opposite directions normal to the layers (Putnis, 1992). The two structures differ in how these layers are stacked. In cristobalite, the layers all have the same orientation, and neighbouring layers are displaced
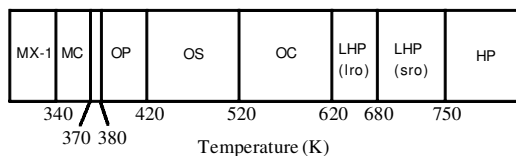

FIG. 1. Equilibrium sequence of phase transitions in tridymite. HP is the ideal high-temperature hexagonal phase (space group $P6_3/mmc$); LHP is a lower-temperature hexagonal phase (space group $P6_322$), which Cellai *et al.* (1994) assign to two distinct phases, one with long-range order (lro) of the apical Si–O bonds and one with short-range order (sro) of these bonds; OC is a C-centred orthorhombic phase (space group $C222_1$); OS is a modulated form of the orthorhombic OC phase; OP is the primitive orthorhombic phase (space group $P2_12_12_1$), which is a $3 \times 1 \times 1$ supercell of the OC phase; MC is a monoclinic phase (space group Cc), and MX-1 is a triclinic modulation of the MC structure.
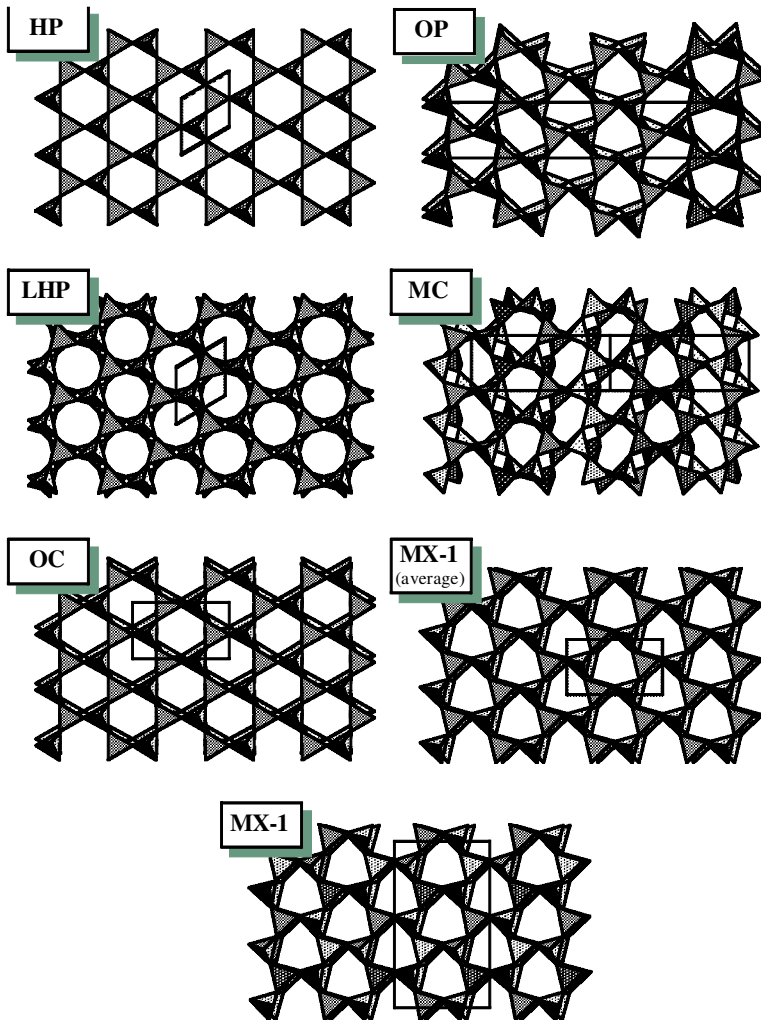
* E-mail: martin@esc.cam.ac.uk

FIG. 2. Crystal structures of tridymite phases; nomenclature is given in the caption to Fig. 1. The projection is down the common [001] direction of the aristotype HP structure.

along a direction within the layers relative to each other in order to provide a linkage between the tetrahedra. The periodicity involves three layers, and the final structure is face-centred cubic. On the other hand, alternative layers in tridymite are rotated by 180° relative to each other in order to provide the linkage between the tetrahedra, and the periodicity involves two layers. This gives a hexagonal crystal structure. In both cases the resultant crystal structures can be viewed as being infinite frameworks of corner-linked tetrahedra, with all tetrahedra forming part of the one

framework, and with no non-bridging Si–O bonds.

In this idealized view of the crystal structures of the two materials, the Si–O–Si bonds are straight, whereas it is commonly found in aluminosilicates that the angle subtended by this type of bond is nearer 145°. However, in both cristobalite and tridymite the idealized structures are found to be good representations of the average structures of the high-temperature phases. Thermal displacement parameters measured by X-ray or neutron diffraction show

large displacements of the O atoms in the plane normal to the idealized Si–O–Si bonds (e.g. Schmahl *et al*., 1992). This suggests that on an instantaneous time scale there is considerable bending of the Si–O–Si bonds but in a way that gives dynamic structural disorder on a short length scale. This aspect of the crystal structure has been studied in some detail in β-cristobalite from both experimental (Schmahl *et al*., 1992; Swainson and Dove, 1993; Dove *et al*., 1997) and theoretical (Swainson and Dove, 1995; Hammonds *et al*., 1996; Gambhir *et al*., 1999) perspectives. It is not likely that this disorder can persist to low temperatures, and the solution is for the crystal structure to distort through a displacive phase transition, giving a lower-symmetry structure with non-linear Si–O–Si bonds. In the case of cristobalite, there is only one phase transition on cooling, to a tetragonal structure with Si–O–Si bond angles nearer the usual value of 145°. In the case of tridymite there is a sequence of displacive phase transitions on cooling, and some of the crystal structures of the intermediate phases still have the idealized average linear Si–O–Si bonds.

The purpose of the present paper is to present some results from studies of the phase transitions in tridymite, which shed some light on the origin of the remarkable sequence of phase transitions, and on the nature of the high-temperature phases. This involves three approaches, which are covered in the following three sections of this paper, namely a theoretical survey using the Rigid Unit Mode model, a joint computational and experimental study using neutron total scattering measurements and reverse Monte Carlo analysis, and a computational study using molecular dynamics simulation.

'Rigid Unit Mode' analysis

Basics of the 'Rigid Unit Mode' model

The 'Rigid Unit Mode' model is a simple approach – at least in principle, although the implementation is not so trivial – which can give insights into many aspects of the stability of framework structures (Hammonds *et al*., 1996). Rigid unit modes (RUMs) are normal modes of the crystal in which the framework is able to flex without the tetrahedra distorting. The joints between two tetrahedra are reasonably flexible, requiring little energy to rotate two tetrahedra about the linkage pivot (Fig. 3). On the other hand, a reasonably large energy is required to

distort the tetrahedra. This gives rise to a range of vibrational frequencies. In quartz, the vibrations that involve stretching of the Si–O bonds have frequencies as high as ~40 THz (Strauch and Dorner, 1993), whereas the RUMs have frequencies of order of 0–1 THz (Swainson and Dove, 1993; Dove *et al*., 1995*a*).

Because of their low energies, RUMs are natural candidates for the vibrations that can act as the soft modes associated with displacive phase transitions (Giddy *et al*., 1993; Dove *et al*., 1995*a*; Hammonds *et al*., 1996; Dove, 1997). This point has been documented in detail for the phase transitions in quartz (Vallade *et al*., 1992), cristobalite (Swainson and Dove, 1993; Hammonds *et al*., 1996) and other silicates (Dove *et al*., 1995*a*; Hammonds *et al*., 1996). What usually happens is that when a RUM distortion is imposed on a crystal structure, leading to a lowering of the symmetry, many of the other RUMs can no longer exist as RUMs, and instead will obtain a non-zero frequency (Hammonds *et al*., 1996). This has been measured experimentally in the case of quartz (Boysen *et al*., 1980; see discussion in Hammonds *et al*., 1996). As a result, there is a much smaller number of possible low-energy deformations in the low-temperature phases. Moreover, in the distorted low-temperature phase, there is often a large reduction in volume and the Si–O–Si bonds angles are able to have usual values, so there is also little driving force for further phase transitions (Dove *et al*., 1995*a*).

It is possible to calculate the number of RUMs for any wave vector in a crystalline material using an algorithm called the "split-atom method" (Giddy *et al*., 1993; Hammonds *et al*., 1994).
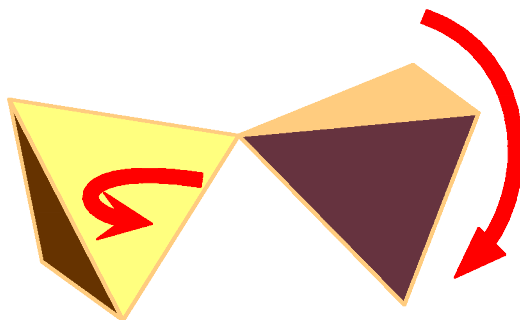

FIG. 3. Two tetrahedra joined at corners, showing types of low-energy motions that do not require distortions of the tetrahedra.

This involves representing each oxygen atom shared between two tetrahedra as a pair of atoms (the "split atoms") with a spring of zero equilibrium length holding the pair of split atoms together. Any distortion of the framework structure that does not require deformation of the tetrahedra will correspond to the movements of the rigid tetrahedra that does not open up the split-atom springs. Formally the stiffness of a split-atom spring is representative (at least to first order) of the stiffness of the tetrahedra – a large force exerted when opening up a pair of split atoms is equivalent to distorting the two tetrahedra. If the only forces included in a model of a crystalline silicate are those associated with the split-atom spring, and all other inter-tetrahedral interactions are neglected, a RUM distortion will cost zero energy. This approach has been implemented within the formalism of molecular lattice dynamics, in which the individual tetrahedra are treated as separate rigid molecular entities with translational and rotational degrees of freedom (Giddy *et al*., 1993; Hammonds *et al*., 1994). In this approach the frequencies of all vibrations are computed for a given wave vector. If one of the vibrations at this wave vector is a RUM, it will have zero frequency. All other vibrations will have values of frequency (actually the square of the frequency) that are determined by the extent to which the vibrational motions open up the split atoms, i.e. the extent to which the vibrational motions cause distortions of the tetrahedra. In practice the calculation is performed for a range of wave vectors to determine the distribution of RUMs in reciprocal space (Pryde and Dove, in prep.; Dove *et al*., 1999).

Rigid Unit Modes in tridymite

The RUMs have been deduced for a number of the phases of tridymite. Results for the high-symmetry hexagonal phase are given in Table 1 with respect to the RUM wave vectors that lie on special points, lines or planes in reciprocal space. Table 1 only gives part of the story, albeit a very important part with regards to the phase transitions, and to which we will return shortly. We have found that in tridymite there are also RUMs with wave vectors lying on exotic curved surfaces in reciprocal space (Dove *et al*., 1995*b*), and these curved surfaces for the HP, LHP and orthorhombic phases are represented in Fig. 4. The existence of RUM surfaces is not as uncommon as was once thought, and similar curved surfaces have been found for a number of aluminosilicates (Pryde and Dove, in prep.; Dove *et al*., 1999; a gallery of RUM surfaces can be found on the world wide web at http://www.esc.cam.ac.uk/rums). However, the curved surfaces of RUMs in the high-temperature phase of tridymite were the first to be discovered, initially by electron diffraction (Withers *et al*., 1994), and subsequently confirmed by detailed calculations (Dove *et al*., 1995*b*).

One important aspect of the RUM spectra for tridymite as shown by Fig. 4 is that the number of RUMs does not significantly decrease on lowering the symmetry through the phase transitions. This is unlike the case of cristobalite (Hammonds *et al*., 1996), and it ensures that there remains a significant number of possible low-energy distortions in the lower-symmetry phases. Moreover, it is found experimentally that the phase transitions do not involve large changes in volume, as

TABLE 1. Rigid unit modes for different special wave vectors in HP tridymite: *A*, non-degenerate; *E*, doubly-degenerate; *T*, triply-degenerate; *F*, quadruply-degenerate (from Hammonds *et al*., 1996).

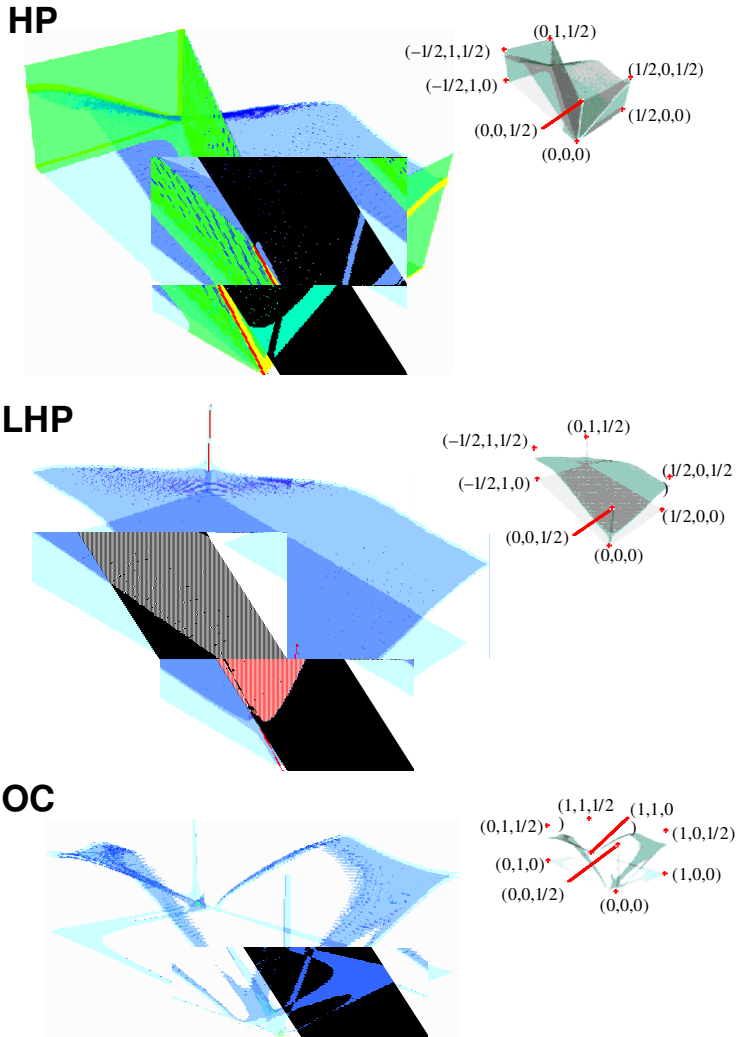| Special points			Special lines			Special planes	
γ	$(0,0,0)$	$2A + 2E$	Σ	$(\xi,0,0)$	$3A$	$(\xi,\zeta,0)$	A
M	$(\frac{1}{2},0,0)$	$3A$	Λ	$(\xi,\xi,0)$	A	$(\xi,0,\zeta)$	$2A$
K	$(\frac{1}{3},\frac{1}{3},0)$	A	Δ	$(0,0,\xi)$	$2A + 2E$		
A	$(0,0,\frac{1}{2})$	$E + F$	R	$(\xi,0,\frac{1}{2})$	E		
L	$(\frac{1}{2},0,\frac{1}{2})$	E	T	$(\frac{1}{2}-\xi,2\xi,0)$	A		
H	$(\frac{1}{3},\frac{1}{3},\frac{1}{2})$	$2A$	U	$(\frac{1}{2},0,\xi)$	$2A$		

FIG. 4. Exotic curved surfaces of wave vectors of RUMs in the reciprocal spaces of the HP, LHP and OC phases of tridymite. The small inset gives the key to special points in reciprocal space.

highlighted in Fig. 5, and some of the high-temperature phases retain some linear Si−O−Si bonds. The first point suggests that there are only small differences in energy between different phases, and the second point implies that there is still a large driving force for additional phase transitions in the phases below the highest-temperature phase. These results go a long way to explaining the large number of displacive phase transitions in tridymite as compared to other silicates such as cristobalite.

The RUM analysis can be quantified further. We have correlated the changes in symmetry at each phase transition with the symmetries of the RUMs in each of the parent structures, and have been able to deduce the phase transition sequences. The results of this analysis are given in Fig. 6. It can be seen that there are at least three distinct sequences of displacive phase transitions starting from the parent high-temperature hexagonal phase (Pryde and Dove, 1998). The sequence of displacive phase transitions first
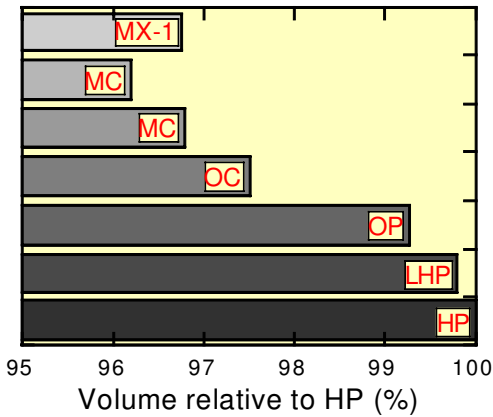
FIG. 5. Graphical representation of the relative volumes of the different phase of tridymite, which highlights the small changes in volume that accompany the different phase transitions.

follows one sequence of RUM distortions, and on further cooling the sequence reverts to one of the other sequences. The family of RUM sequences given in Fig. 6 correlates many of the known phase transitions in tridymite, including some that appear to depend on sample history.
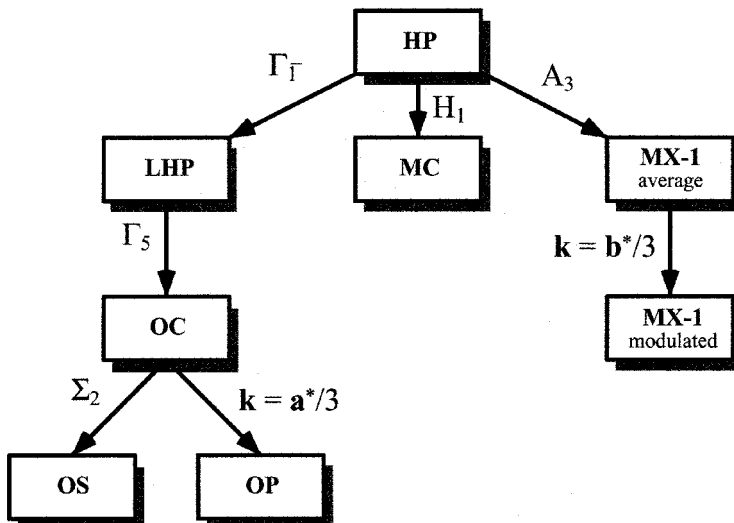
Neutron total scattering measurements and Reverse Monte Carlo analysis

Total scattering experiments

Neutron total scattering experiments involve the measurement of the total diffraction pattern, including both the Bragg peaks and the diffuse scattering. The Bragg scattering gives information about the average positions (or average distribution of positions) of the atoms in the unit cell. On the other hand, the total diffraction pattern gives information about the distribution of the distances between atoms. In the case of disordered materials, this difference is significant. The average structure of the high-temperature phases of tridymite gives linear Si–O–Si bonds, as highlighted earlier. However, the distribution of positions of the oxygen atoms as indicated by refinement of the temperature factors involves considerable motion of each oxygen atom in a plane normal to the Si–Si vector. This is illustrated in Fig. 7. It can be seen that the linear bonds will be shorter than the actual instantaneous bonds, and that in a determination of the average structure, there will be a large distribution of positions of the oxygen atom in a plane normal to the Si–Si vector. It needs to be appreciated that determination of the details of this point is not trivial. In principle the rough

FIG. 6. Phase transition sequences in tridymite, represented by the symmetries of the RUMs that correspond to the distortions though each phase transition. The phases within each sequence have a distinct group-subgroup symmetry representation that is characterized by the symmetry of the RUM distortion.
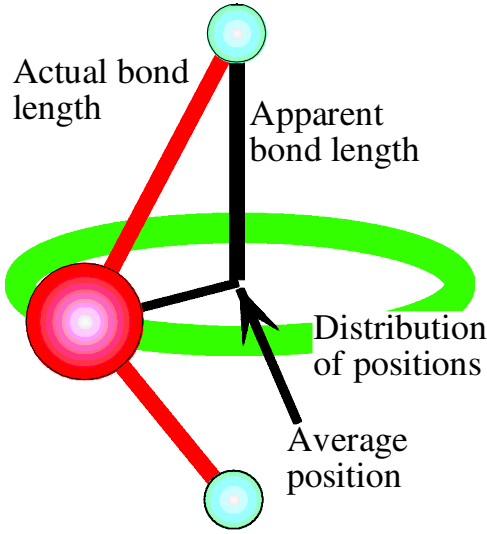
FIG. 7. Illustration of the difference between actual instantaneous interatomic separations and the separations between average positions.

picture emerges naturally from the analysis of the data from Bragg diffraction. However, the resolution in real space is given by $2\pi/Q_{max}$, where Q_{max} is the magnitude of the upper limit of the scattering vector Q in the experiment. For analysis of data from Cu-$K\alpha$ X-radiation, the upper limit on Q gives an intrinsic resolution of only 0.75 Å, which is too poor to enable different models of the disorder to be distinguished. Thus to get a good picture of the nature of the structural disorder it is necessary to obtain diffraction data to much larger values of Q. This is most easily accomplished using time-of-flight neutron diffraction data from a spallation source.

The quantity that is sought in the experiments is the scattering function $S(Q)$. This involves both elastic and inelastic scattering, and is related to the instantaneous relative positions of the atoms. For a given scattering vector $\mathbf{Q}$, $S(\mathbf{Q})$ is related to the atomic positions through

$$S(\mathbf{Q}) = \sum_{j;k} b_j b_k \langle \exp(i\mathbf{Q} \cdot (\mathbf{r}_j - \mathbf{r}_k)) \rangle$$

where $\mathbf{r}_j$ and $\mathbf{r}_k$ are the instantaneous positions of atoms j and k respectively, and the average is over all possible atomic configurations as sampled in an experiment. b_j and b_k are the neutron scattering lengths (the neutron equivalent of the X-ray

atomic scattering factors) of atoms j and k respectively. In a powder diffraction experiment, this expression needs to be averaged over all orientations of $\mathbf{Q}$. This leads to the well-known Debye formula

$$\begin{aligned} S(Q) &= \sum_{jk} b_j b_k \sin(Qr_{jk})/Qr_{jk} \\ &= \sum_j b_j^2 + \sum_{j \neq k} b_j b_k \sin(Qr_{jk})/Qr_{jk} \end{aligned}$$

where $r_{jk} = |\mathbf{r}_j - \mathbf{r}_k|$. Here we have separated the terms involving the same atom twice (the so-called 'self terms') and the terms involving two different atoms. The latter sum implies knowledge of the separations of all the atoms, but instead we are interested only the distribution of these atomic separations. Hence we write the equation for $S(Q)$ in terms of the appropriate distribution function, and now assume normalization with respect to the number of formula units:

$$S(Q) = \sum_m c_m b_m^2 + \\ \sum_{mn} c_m c_n b_m b_n \int_0^\infty 4\pi r^2 g_{mn}(r) \frac{\sin(Qr)}{Qr} \, dr$$

m and n now refer to distinct atom types, each of concentration c_m and c_n respectively. The distribution function $g_{mn}(r)$ is defined such that $4\pi r^2 g_{mn}(r) dr$ gives the average number of atoms of type m lying within a shell of thickness dr and radius r from any atom n. It is common to represent the Fourier transform of $S(Q)$ in terms of

$$T(r) = 4\pi r \sum_{mn} b_m b_n g_{mn}(r)$$

since this is clearly the function within the transform integral and can therefore be said to be the best representation of the direct transformation of experimental data for $S(Q)$.

The neutron scattering data were collected on the LAD diffractometer (now decommissioned; Howells and Hannon, 1999) at the ISIS spallation neutron source, using a polycrystalline sample of tridymite contained within a cylindrical vanadium can. Data were collected up to large values of Q, although for values of Q greater than 50 Å^{-1} there is little significant structure in the data. Data were collected at several temperatures, but here we concentrate on the data from one temperature in the stability field of the high-temperature phase of tridymite.

The raw data were corrected for intrinsic background by subtracting measurements of the background signal and making corrections for the attenuation of the neutron beam by the sample, vanadium can and furnace. A standard silicon sample was used to calibrate the values of $l\sin\theta$ for each detector, where l is the total neutron flight path and θ is half the scattering angle. A standard vanadium sample was used to calibrate detector efficiencies and to normalize the data onto an absolute scale. The final result for $S(Q)$ is shown in Fig. 8.

Constrained Reverse Monte Carlo methods

The data were analysed using the constrained Reverse Monte Carlo refinement method (Keen, 1997, 1998). This is a computer simulation method, in which an initial configuration of atoms of the same density as the real sample is contained within a periodic cell. The positions of the atoms within this configuration are allowed to relax using a Monte Carlo method to move the atoms. Any move that improves the agreement between the calculated and experimental $S(Q)$ is accepted, whereas any move that worsens the agreement is accepted or rejected depending on the outcome of a probability test. The procedure is continued for many steps until the calculated $S(Q)$ only changes within the assumed limits of accuracy. Soft constraints were imposed to ensure that the Si–O tetrahedra were not allowed to break up during the relaxation procedure. At the point at which the calculated $S(Q)$ is in agreement with the experimental data, it is assumed that the configuration is a reasonable representation of the atoms in the real material. This configuration can be analysed to give information on the structure over short length scales.

The $T(r)$ function and the individual $g(r)$ functions obtained from analysis of the RMC configurations are shown in Fig. 9. These functions are remarkably similar to those obtained from β-cristobalite (Dove *et al.*, 1997; Keen and Dove, 1999), which are also shown for comparison. In particular, the Si–O and O–O $g(r)$ functions are consistent with the existence of regular SiO$_4$ tetrahedra with mean Si–O distance of 1.67 Å and mean O–O distance of 2.6 Å. As in the case of β-cristobalite, the Si–O and O–O distances are greater than the distances from the average structure, suggesting that the Si–O bonds are actually tilted away from their average
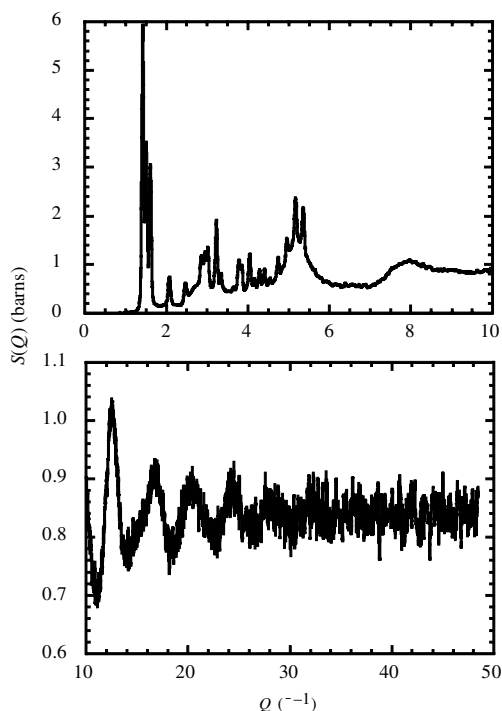

FIG. 8. Neutron scattering $S(Q)$ data for the HP phase of tridymite, drawn over two distinct ranges of Q to highlight the existence of sharp distinct Bragg peaks at lower values of Q and oscillations at larger values of Q.

orientations to give bent Si–O–Si angles. In fact, from the triangle made from the Si–Si vector (mean distance 3.13 Å) and two Si–O vectors (see Fig. 7) we can surmise an average Si–O–Si angle of 141°. This is highlighted in calculations of the two bond orientational distribution functions shown in Fig. 10, where they are also compared with the corresponding distribution functions obtained for β-cristobalite. The orientational distribution function $f(\theta)$ for the Si–O–Si angles give a mean value of the angle of ~140–150°, with a wide and asymmetric distribution of angles. The distribution is very similar to that of β-cristobalite.

The distortions of the structure as seen through the Si–O–Si bond distribution function $f(\theta)$, taken with the fact that the $g(r)$ functions indicate regular SiO$_4$ tetrahedra, suggests that tetrahedra are able to rotate without significant distortions in order to avoid the formation of linear Si–O–Si bonds. This poses the question of how such distortions can arise. In the case of β-cristobalite, several scenarios have been proposed, which are

FIG. 10. Bond angle distribution functions for tridymite obtained from analysis of the RMC configurations. The meaning of the angles in plots a and b are defined by the small cartoons. The corresponding data for β-cristobalite are shown for comparison.
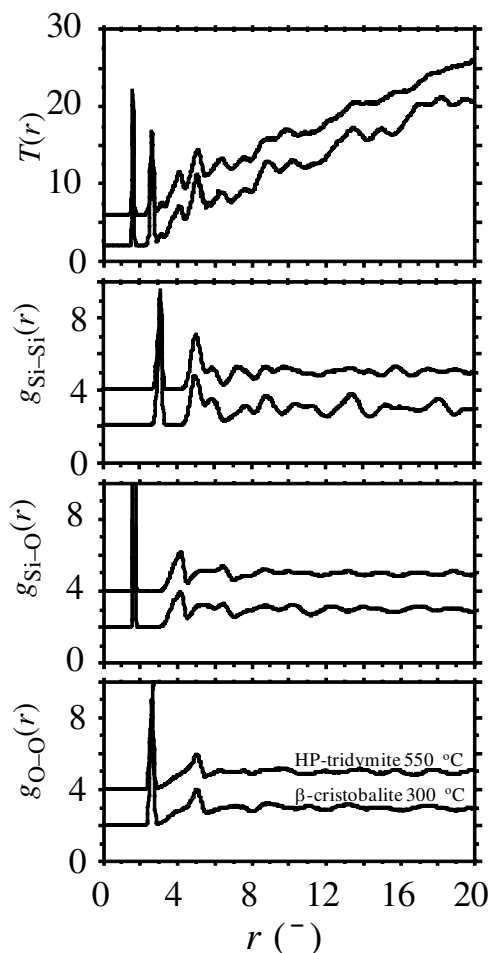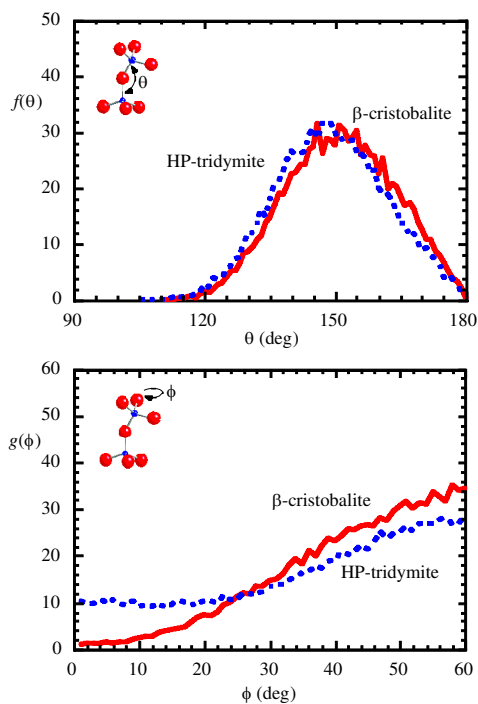
FIG. 9. The overall $T(r)$ function for HP-tridymite obtained by Fourier transform of the experimental $S(Q)$ data, together with the individual pair distribution functions $g(r)$ obtained from the RMC simulations. The corresponding data for β-cristobalite are shown for comparison, in particular to highlight the close similarities.

discussed in detail by Dove *et al.* (1997). Some of these are based on the instantaneous formation of small domains of lower-symmetry structures. An insight into this issue can be obtained by inspection of an instantaneous configuration of tetrahedra, a layer of which is shown in Fig. 11. It is apparent from this figure that the rotations of the tetrahedra do not involve formation of domains. The distortions of the hexagonal rings

are large, but there is no apparent correlation between the distortions of neighbouring rings. A similar picture has been obtained from RMC configurations of β-cristobalite (Keen, 1998; Dove *et al.*, 1998; Keen and Dove, 1999). The distribution of orientations is highlighted in the orientational distribution function $g(\phi)$ shown in Fig. 10, which gives the distribution of relative torsional orientations of neighbouring tetrahedra. The tridymite structure has pairs of neighbouring SiO$_4$ tetrahedra in two relative orientations, 1/4 of the pairs having an angle 0° and 3/4 of the pairs having an angle 60° (unlike β-cristobalite, which has only relative orientations of 60°). The disorder is seen as a wide distribution of these angles.

In the case of β-cristobalite we proposed that the disorder arises from the instantaneous superposition of many RUMs, leading to a dynamically disordered state (Swainson and Dove, 1993, 1995). This is possible because there is a large
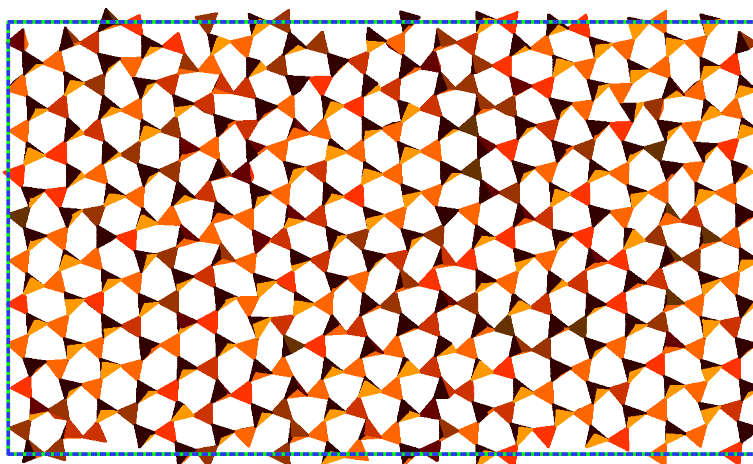
FIG. 11. Instantaneous snapshot of the SiO_4 tetrahedra in a single (001) layer of HP-tridymite obtained from the RMC simulations. The important point to note is that there is considerable orientational disorder of the tetrahedra without the formation of small ordered patches.

number of these modes. In fact, we do not need to take into account only the RUMs at the precise wave vectors, but the modes on the same vibrational dispersion surface in the vicinity of the RUM wave vectors will have very low frequencies and can contribute to the formation of the dynamic disorder. The RUM interpretation of the dynamic disorder in β-cristobalite has been developed in some detail through a series of experimental (Swainson and Dove, 1993; Dove *et al*., 1997) and theoretical studies (Swainson and Dove, 1995; Hammonds *et al*., 1996), and the results can be applied directly to the case of tridymite.

Molecular dynamics simulations

Model rigid-ion interatomic potentials

The final approach in our study of tridymite is to use molecular dynamics simulations to consider in more detail the nature of the high-temperature phase, following a similar application in the study of β-cristobalite (Swainson and Dove, 1995). The development of these calculations in this study of tridymite proved particularly illuminating. We investigated a number of model 'rigid ion' interatomic potentials, which are listed and labelled in Table 2. Some of these models were derived empirically, some from quantum

TABLE 2. Source of the model interatomic potentials, which are defined with reference to their source.

Model	Source	Notes
DK84	Dempsey and Kawamura (1984)	Empirical model
KFBS91a	Kramer *et al*. (1991)	Fitted to quantum mechanical energies + empirical adjustment
KFBS91b	Kramer *et al*. (1991)	Fitted to quantum mechanical energies
LG87a	Lasaga and Gibbs (1987)	Fitted to quantum mechanical energies
LG87b	Lasaga and Gibbs (1987)	Fitted to quantum mechanical energies + empirical adjustment
SA91	Scamehorn and Angell (1991)	Empirical model
TTAM88	Tsuneyuki *et al*. (1988)	Fitted to quantum mechanical energies
TTAM89	Tsuneyuki *et al*. (1989)	Fitted to quantum mechanical energies
Shell	Sanders *et al*. (1984)	Empirical model

TABLE 3. The results of static lattice simulations of HP tridymite using eight different rigid ion potential models and the shell model potential. The lattice energy, cell volume and *a* and *c* lattice parameters are given in each case. Some of the simulated structures had optic phonon modes with imaginary frequencies at the Γ-point. For those structures which did not, the frequencies of the lowest optic phonon modes are given in italics instead. The phonon calculations were performed at a wave vector slightly away from $\mathbf{k} = 0$ in order to ensure the correct TO/LO splitting of the optic phonon branches.

Model	E (eV)	V (Å^{-3})	a (Å)	c (Å)	ω_Γ (THz)
DK84	−565.93	190.335	5.124	8.370	*2.62, 2.62*
KFBS91a	−232.55	202.931	5.236	8.546	1.20*i*, 1.20*i*, 0.72*i*, 0.46*i*
KFBS91b	−162.58	217.392	5.358	8.744	0.01*i*, 0.01*i*
LG87a	−514.24	206.115	5.262	8.596	*2.48, 2.48*
LG87b	−31.91	202.384	5.231	8.542	*0.58, 0.58*
SA91	−513.55	222.555	5.399	8.816	*2.18, 2.18*
TTAM88	−214.16	216.880	5.354	8.736	0.98*i*, 0.98*i*
TTAM89	−216.70	208.642	5.285	8.625	0.99*i*, 0.99*i*
Shell	−514.52	195.285	5.169	8.439	3.46*i*, 3.41*i*, 3.18*i*, 3.18*i*, 1.68*i*, 1.68*i*

mechanics calculations, and some from quantum mechanics calculations with empirical corrections. Our first tests were based on static lattice energy and lattice dynamics calculations, using the program GULP (Gale, 1997). We took the view that a good model for tridymite should be able to reproduce at least some aspects of the higher-temperature phase transitions. The first test is that the static lattice energy computed for the OC phase should be lower than for the LHP phase, which in turn should be lower than that

computed for the HP phase. Together with this we addressed the issue of whether the models gave appropriate behaviour in harmonic lattice dynamics calculations on the HP and LHP phases. Specifically, a good model should predict the correct soft modes for the displacive phase transitions, which in a harmonic lattice dynamics calculation will give rise to modes of negative squared frequency (i.e. imaginary frequency) at the appropriate phonon wave vectors. For the phase transitions from both the

TABLE 4. The results of static lattice simulations of LHP tridymite using the four rigid-ion potential models which showed zone centre soft mode instabilities in the HP phase, and the shell model potential. The lattice energy, cell volume and *a* and *c* lattice parameters are given in each case along with the *x* coordinate of one of the two symmetrically independent oxygen atoms. This coordinate is constrained to be 0.5 in the HP phase by symmetry, but is free to vary in the LHP phase. The phonon frequencies of zone centre soft optic modes are given with the exception of the KFBS91b model which had none and so the frequencies of the lowest optic phonon modes are given in italics instead.

Model	E (eV)	V (Å^{-3})	a (Å)	c (Å)	x(O)	ω_γ (THz)
KFBS91a	−232.55	200.426	5.202	8.553	0.468	1.19*i*, 1.19*i*
KFBS91b	−162.58	217.400	5.358	8.744	0.500	*0.11, 0.11*
TTAM88	−214.16	216.883	5.354	8.736	0.500	0.98*i*, 0.98*i*
TTAM89	−216.70	208.644	5.285	8.625	0.500	0.99*i*, 0.99*i*
Shell	−514.76	182.316	4.982	8.483	0.409	0.62*i*, 0.62*i*

TABLE 5. The results of static lattice simulations of OC tridymite using the four rigid ion potential models which showed zone centre soft mode instabilities in the HP phase, and the shell model potential. The lattice energy, primitive cell volume and *a*, *b* and *c* lattice parameters are given in each case. Also included for each model is the ratio of the primitive cell volumes of the OC and HP phases as a percentage.

Model	E (eV)	V (Å^{-3})	a (Å)	b (Å)	c (Å)	V_{OC}/V_{HP} (%)
KFBS91a	−232.77	175.376	8.972	4.897	7.983	86.4
KFBS91b	−162.58	217.043	9.283	5.353	8.735	99.8
TTAM88	−214.33	189.555	9.261	5.034	8.132	87.4
TTAM89	−216.84	185.424	9.153	5.008	8.090	88.9
Shell	−514.68	181.629	8.964	4.974	8.148	93.0

HP and LHP phases, the soft modes should occur at zero wave vector ($\mathbf{k} = 0$), and ideally would correspond to those predicted by the RUM model (two single soft modes, and two sets of double-degenerate soft modes). By analogy with harmonic lattice dynamics calculations for β-cristobalite (Dove *et al.*, 1993), we might expect the harmonic lattice dynamics calculations to give negative squared frequencies for all or many of the RUM wave vectors in addition to the wave vector specifically associated with the observed phase transition. The results for these tests are given in Tables 3–5.

It can be seen from the results that these simple lattice energy and harmonic lattice dynamics calculations tests left us with only three models that gave the possibilities for $\mathbf{k} = 0$ HP→LHP→OC displacive phase transitions, namely one of the models of Kramer *et al.* (1991) and the two models of Tsuneyuki *et al.* (1988, 1989). Although the tests have indicated that the experimental sequence of displacive phase transitions is possible with each of these remaining models, the harmonic lattice dynamics calculations also gave potential soft modes at additional wave vectors, in line with the comments given earlier. Because of this, the simple tests cannot predict whether the experimental sequence of displacive phase transitions will be preferred over alternative sequences of phase transitions in any model. Thus we used molecular dynamics simulation methods to determine the most favourable sequence of phase transitions on cooling from the HP phase in each of the remaining models.

The molecular dynamics simulation calculations were performed using the parallel code

DLPOLY (Smith and Forester, 1996). In all cases our simulation samples contained 2592 ions with periodic boundary conditions. The simulations were performed with the NPT ensemble to allow for relaxation of strain at each temperature. Simulations were performed by either cooling from the HP phase, or heating from an initial OC structure.

The molecular dynamics simulations on the three remaining models showed that they all predicted phase transition sequences different from the experimental HP→LHP→OC sequence, and the new phases were those associated with soft modes with non-zero wave vectors. For example, the TAM88 model gave rise to a
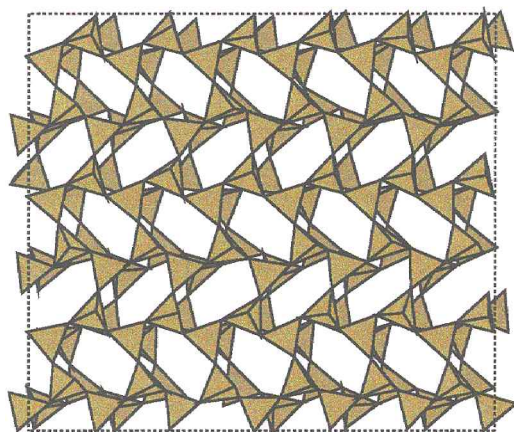

FIG. 12. Instantaneous layer of SiO$_4$ tetrahedra taken from the structure obtained by molecular dynamics simulation using the TAS88 model at low temperatures.
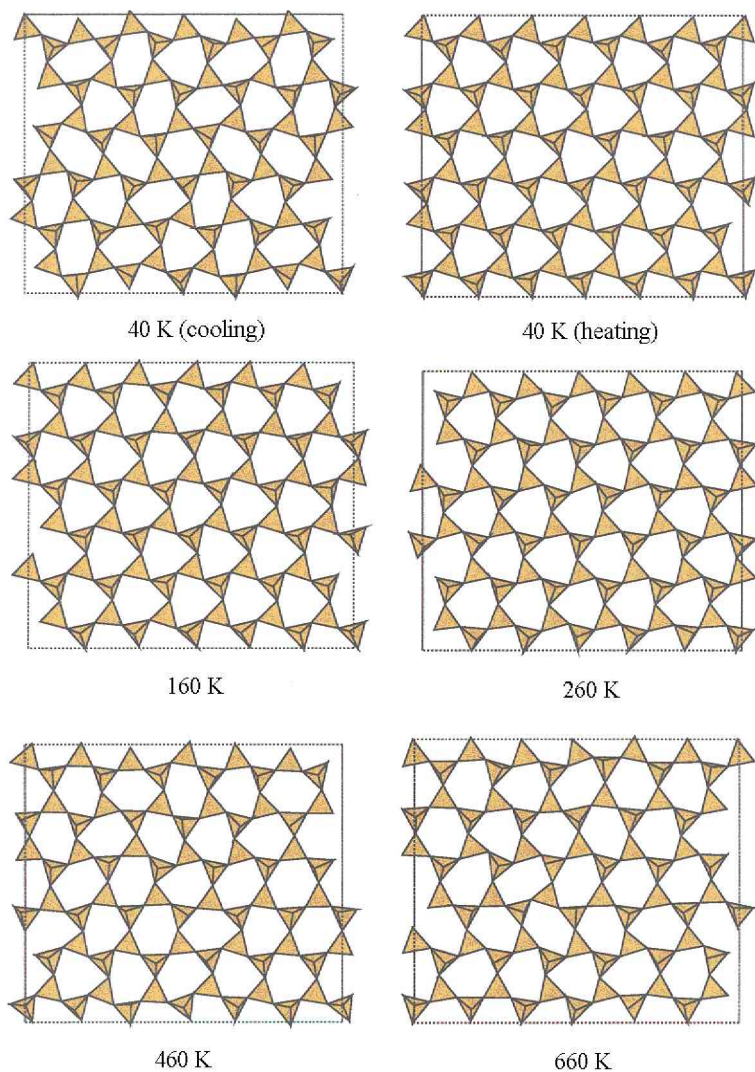
40 K (cooling)

40 K (heating)

160 K

260 K

460 K

660 K

FIG. 13. Instantaneous layers of SiO$_4$ tetrahedra taken from the structures obtained by molecular dynamics simulation using the shell model potentials at various temperatures in both heating and cooling runs.

sheared structure on cooling from the HP phase, as shown in Fig. 12.

We were forced to conclude that none of the rigid-ion models we tested were able to reproduce the sequence of phase transitions on cooling from the HP phase. Now we know that in all empirical (and indeed quantum mechanical) models the forces between atoms are inadequate in specific respects, and that to simulate displacive phase transitions is a particularly challenging require-

ment of any model, but we also know from general experience of model interatomic forces that we could have expected more success with at least one of the models. For this reason, we believe that the failure of all rigid ion models to reproduce the sequence of displacive phase transitions in tridymite has its own message about tridymite over and above the trivial message that it is hard to simulate displacive phase transitions. For example, the model of
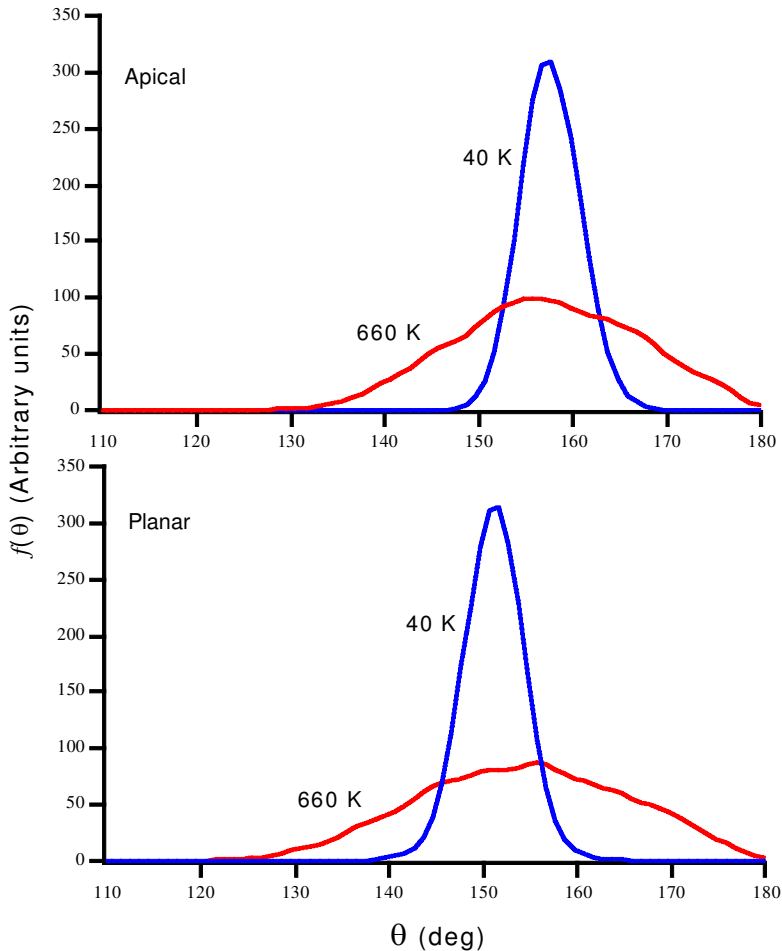
F<small>IG</small>. 14. Si−O−Si bond orientational distribution function $f(\theta)$ for HP-tridymite obtained from the molecular dynamics simulations using the shell model potential, to be compared with the experimental function given in Fig. 10.

Tsuneyuki *et al*. (1988) has been successfully used to simulate the displacive phase transitions in both quartz (Tsuneyuki *et al*., 1990) and cristobalite (Swainson and Dove, 1995). We believe that the difficulties in simulating the sequence of phase transitions in tridymite are consistent with the conclusions drawn earlier in this paper, namely that there are many possible phase transition sequences allowed by the wide range of RUMs to act as potential soft modes, and that the small changes in volume through any of the phase transitions implies that the differences in energy between different phases are small.

Molecular dynamics simulations with shell-model potentials

Although none of the rigid-ion models were sufficiently accurate to use in the molecular dynamics simulations, we did achieve more success with the shell model of Sanders *et al*. (1984). This gave satisfactory results in the static lattice energy and harmonic lattice dynamics calculations (giving two single soft modes and two sets of double-degenerate soft modes), and the molecular dynamics simulations gave a $\mathbf{k} = 0$ displacive phase transition on cooling from the HP phase. The sequence of phase transitions in
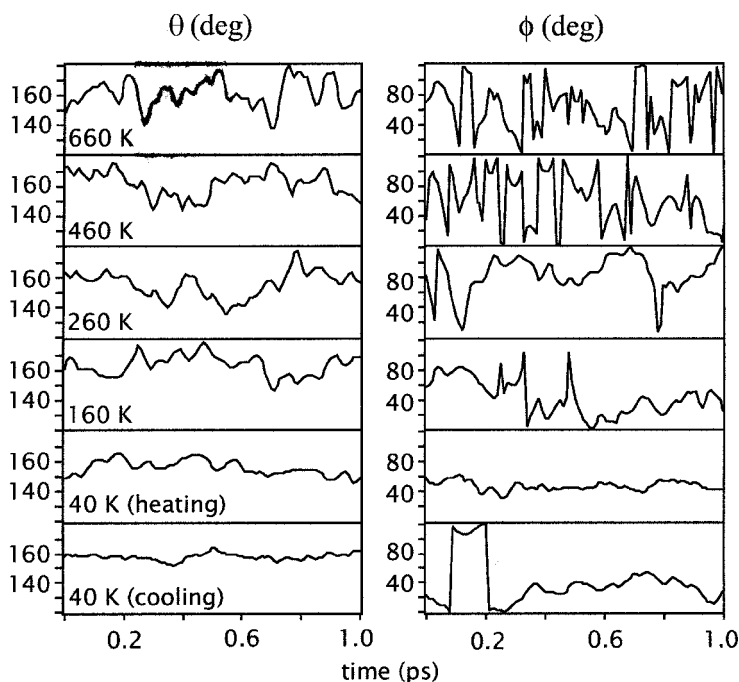
FIG. 15. Time-dependence of the apical bond orientational angles θ and ϕ as defined in Fig. 10 for pairs of SiO_4 tetrahedra.

the molecular dynamics simulations did not match the experimental sequence beyond this point, but at least the model appears to capture some aspects of the real behaviour. Because of this we felt that the model would be appropriate for the investigation of the properties of the high-temperature phase, which could give information that complements the RMC analysis.

Figure 13 shows some configurations of the molecular dynamics simulations at a few temperatures. The high-temperature configurations bear a strong resemblance to those generated by the RMC method (Fig. 11). We include also the low-temperature structures to show how the system orders, and note that the structure obtained on cooling is not the same as the starting structure in the heating runs. The distributions of the angles of the $Si-O-Si$ bonds from these configurations are shown in Fig. 14. Here we have separated the bonds lying close to the [001] axis (apical) from those lying in the 6-membered rings in the $a-b$ plane (planar). The distribution of bond angles is similar to that found in the RMC analysis and given in Fig. 10 (although the latter have been averaged over both types of bond angles).

The molecular dynamics simulations are able to provide direct information about the dynamic behaviour of the atoms. In Fig. 15 we show the time-dependence of the apical $Si-O-Si$ angles for a single bond lying along [001], together with the corresponding torsional angle as defined in Fig. 10. The results show that at high temperatures there are large tetrahedral reorientations over time scales of <1 ps. This highlights the fact that the structural disorder associated with attempts to distort the $Si-O-Si$ bonds is dynamic rather than static. This result is very similar to that found in the simulation study of β-cristobalite (Swainson and Dove, 1995), and further illustrates the similarities of the structural disorder in the high-temperature phases of these two polymorphs of silica.

Discussion

The main thrust of this work has been twofold: first, to facilitate an understanding of the sequences of displacive phase transitions in tridymite, and second to give an understanding of the nature of the high-temperature phase. The

results of the RUM model clearly show that the complex sequences of phase transitions can be fully accounted for by the existence of RUMs, and the facts that the individual phase transitions do not remove too many RUMs nor give a drastic change to the volume, allow several successive phase transitions to occur. This contrasts with the case in many other framework silicates, where phase transitions involve large changes in volume and big reductions in the number of RUMs, and correspondingly have fewer phase transitions on further cooling.

The experimental diffraction data analysed by the constrained RMC refinement method and the MDS results paint a picture of a truly disordered high-temperature phase. There is a wide distribution of orientations of the SiO_4 tetrahedra, allowing the bending of the $Si-O-Si$ bonds which appear to be linear in the idealized average structure. This distribution of orientations is facilitated by the large number of RUMs, which can combine dynamically across all RUM wave vectors to create considerable disorder on a short length scale. This is very similar to the situation in β-cristobalite, as shown by the same combination of experimental and computational methods.

Acknowledgements

References

Boysen, H., Dorner, B., Frey, F. and Grimm, H. (1980) Dynamic structure determination for two interacting modes at the M-point in α- and β-quartz by inelastic neutron scattering. *J. Physics C: Solid State Physics*, **13**, 6127–46.

Cellai, D., Carpenter, M.A., Wruck, B. and Salje, E.K.H. (1994) Characterization of high-temperature phase transitions in single crystals of Steinbach tridymite. *Amer. Mineral.,* **79**, 606–614.

de Dombal, R.F. and Carpenter, M.A. (1993) High-temperature phase transitions in Steinbach tridymite. *Eur. J. Mineral.,* **5**, 607–622.

Dempsey, M.J. and Kawamura, K. (1984) Molecular dynamics simulation of the structure of aluminosilicate melts. Pp. 49–56 in: *Progress in Experimental Petrology* (C.M.B. Henderson, editor). Natural Environment Research Council, Manchester.

Dove, M.T. (1997) Silicates and soft modes. Pp. 349–83 in: *Amorphous Insulators and Semiconductors* (M.F. Thorpe and M.I. Mitkova, editors). NATO ASI series **3**. High Technology, **23**. Kluwer, Amsterdam.

Dove, M.T., Giddy, A.P. and Heine, V. (1993) Rigid unit mode model of displacive phase transitions in framework silicates. *Trans. Am. Crystallogr. Assoc.,* **27**, 65–74.

Dove, M.T., Heine, V. and Hammonds, K.D. (1995*a*) Rigid unit modes in framework silicates. *Mineral. Mag.,* **59**, 629–39.

Dove, M.T., Hammonds, K.D., Heine, V., Withers, R.L., Xiao, Y. and Kirkpatrick, R.J. (1995*b*) Rigid unit modes in the high-temperature phase of SiO_2 tridymite: Calculations and electron diffraction. *Phys. Chem. Min.,* **23**, 56–62.

Dove, M.T., Keen, D.A., Hannon, A.C. and Swainson, I.P. (1997) Direct measurement of the $Si-O$ bond length and orientational disorder in β-cristobalite. *Phys. Chem. Min.,* **24**, 311–17.

Dove, M.T., Hammonds, K.D. and Trachenko, K. (1999) Floppy modes in crystalline and amorphous silicates. Pp. 217–38 in: *Rigidity Theory and Applications* (M.F. Thorpe and P.M. Duxbury, editors). Plenum, New York.

Dove, M.T., Heine, V., Hammonds, K.D., Gambhir, M. and Pryde, A.K.A. (1998) Short-range disorder and long-range order: implications of the 'Rigid Unit Mode' model. Pp. 253–72 in: *Local Structure from Diffraction* (M.F. Thorpe and S. Billinge, editors). Plenum, New York.

Gale, J.D. (1997) GULP: A computer program for the symmetry-adapted simulation of solids. *J. Chem. Soc.: Faraday Trans.,* **93**, 629–37.

Gambhir, M., Dove, M.T. and Heine, V. (1999) Rigid Unit Modes and dynamic disorder: SiO_2 cristobalite and quartz. *Phys. Chem. Min.,* **26**, 484–95.

Giddy, A.P., Dove, M.T., Pawley, G.S. and Heine, V. (1993) The determination of rigid unit modes as potential soft modes for displacive phase transitions in framework crystal structures. *Acta Crystallogr.,* **A49**, 697–703.

Hammonds, K.D., Dove, M.T., Giddy, A.P. and Heine, V. (1994) CRUSH: A FORTRAN program for the analysis of the rigid unit mode spectrum of a framework structure. *Amer. Mineral.,* **79**, 1207–9.

Hammonds, K.D., Dove, M.T., Giddy, A.P., Heine, V. and Winkler, B. (1996) Rigid unit phonon modes and structural phase transitions in framework silicates. *Amer. Mineral.,* **81**, 1057–79.

Howells, W.S. and Hannon, A.C. (1999) LAD,

1982 – 1998: the first ISIS diffractometer. *J. Physics: Condensed Matter*, **11**, 9127 – 38.

Keen, D.A. (1997) Refining disordered structural models using reverse Monte Carlo methods: Application to vitreous silica. *Phase Transitions*, **61**, 109 – 24.

Keen, D.A. (1998) Reverse Monte Carlo refinement of disordered silica phases. Pp. 109 – 19 in: *Local Structure from Diffraction* (S.J.L. Billinge and M.F. Thorpe, editors). Plenum, New York.

Keen, D.A. and Dove, M.T. (1999) Local structures of amorphous and crystalline phases of silica, SiO_2, by neutron total scattering. *J. Physics: Condensed Matter*, **11**, 9263 – 73.

Kramer, G.J., Farragher, N.P., van Beest, B.W.H. and van Santen, R.A. (1991) Interatomic force fields for silicates, aluminophosphates and zeolites: Derivation based on *ab initio* calculations. *Phys. Rev.,* **B43**, 5068 – 79.

Lasaga, A.C. and Gibbs, G.V. (1987) Applications of quantum mechanical potential surfaces to mineral physics calculations. *Phys. Chem. Min.,* **14**, 107 – 17.

Pryde, A.K.A. and Dove, M.T. (1998) On the sequence of phase transitions in tridymite. *Phys. Chem. Min.*, **26**, 171 – 9.

Sanders, M.J., Leslie, M. and Catlow, C.R.A. (1984) Interatomic potentials for SiO_2. *J. Chem. Soc.: Chem. Comm.,* 1271 – 3.

Scamehorn, C.A. and Angell, C.A. (1991) Viscosity-temperature relations and structure in fully polymerized aluminosilicate melts from ion dynamics simulations. *Geochem. Cosmochim. Acta,* **55**, 721 – 30.

Schmahl, W.W., Swainson, I.P., Dove, M.T. and Graeme-Barber, A. (1992) Landau free energy and order parameter behaviour of the $\alpha – \beta$ phase transition in cristobalite. *Zeits. Kristallogr.,* **201**, 125 – 45.

Smith, W. and Forester, T.R. (1996) DL_POLY_2.0 – A general purpose parallel molecular dynamics simulation package. *J. Molecular Graphics*, **14**, 136 – 41.

Strauch, D. and Dorner, B. (1993) Lattice dynamics of α-quartz. 1. Experiment. *J. Physics: Cond. Matt.*, **5**, 6149 – 54.

Swainson, I.P. and Dove, M.T. (1993) Low-frequency floppy modes in β-cristobalite. *Phys. Rev. Lett.*, **71**, 193 – 6.

Swainson, I.P. and Dove, M.T. (1995) Molecular dynamics simulation of α-cristobalite and β-cristobalite. *J. Physics: Cond. Matt.*, **7**, 1771 – 88.

Tsuneyuki, S., Tsukada, M., Aoki, H. and Matsui, Y. (1988) First principles interatomic potential of silica applied to molecular dynamics. *Phys. Rev. Lett.,* **61**, 869 – 72.

Tsuneyuki, S., Tsukada, M., Aoki, H. and Matsui, Y. (1989) New pressure-induced structural transformations in silica obtained by computer simulation. *Nature,* **339**, 209 – 11.

Tsuneyuki, S., Aoki, H., Tsukada, M. and Matsui, Y. (1990) Molecular dynamics study of the α to β structural phase transition of quartz. *Phys. Rev. Lett.,* **64**, 776 – 9.

Vallade, M., Berge, B. and Dolino, G. (1992) Origin of the incommensurate phase of quartz: II. Interpretation of inelastic neutron scattering data. *J. de Physique I,* **2**, 1481 – 95.

Withers, R.L., Thompson, J.G., Xiao, Y. and Kirkpatrick, R.J. (1994) An electron diffraction study of the polymorphs of SiO_2-tridymite. *Phys. Chem. Min.*, **21**, 421 – 33.